EPJ Web of Conferences **289**, 01005 (2023) https://doi.org/10.1051/epjconf/202328901005
FCCP2022

Leading hadronic contribution to the muon g-2 from lattice QCD

B. C. Toth[1,*] for the Budapest–Marseille–Wuppertal collaboration

[1] *University of Wuppertal*

Abstract. We compute the leading order hadronic vacuum polarization contribution to the anomalous magnetic moment of the muon. The calculations are performed using four flavors of stout smeared staggered quarks, with quark masses at their physical values. The continuum limit is taken using six different lattice spacings ranging from 0.132 fm down to 0.064 fm. All strong isospin breaking and electromagnetic effects are accounted for to leading order. A controlled infinite volume limit is taken thanks to dedicated simulations performed in box sizes up to 11 fm. Putting all these ingredients together, we find $[(g_\mu - 2)/2]_{\text{LO-HVP}} = 707.5[5.5] \times 10^{-10}$, which has a total uncertainty of 0.8%. Compared to determinations based on the $e^+e^- \to$ hadrons cross section, our result significantly reduces the tension between the standard model prediction for the muon $g-2$ and its experimental value.

1 Introduction

The muon is a 207 times heavier sibling of the electron, it has the same electric charge and spin. Similarly to the electron, the muon has a magnetic moment, which is proportional to its spin and charge, and inversely proportional to twice its mass. The Dirac equation of relativistic quantum mechanics predicts that the constant of proportionality, g_μ, should be 2. However, in quantum field theory this prediction receives small corrections due to vacuum fluctuations. These corrections are quantified by the anomalous magnetic moment $a_\mu = (g_\mu - 2)/2$. It was measured to a precision of 0.54 ppm at the Brookhaven National Laboratory in the early 2000s [1], and was confirmed recently by Fermilab [2].

At this level of precision, all of the interactions of the standard model are relevant. Although the leading contributions are described by quantum electrodynamics (QED), the one that dominates the theory error is induced by the strong interaction and requires solving the highly non-linear equations of quantum chromodynamics (QCD) at low energies. This contribution is determined by the leading-order, hadronic vacuum polarization (LO-HVP), which describes how the propagation of a virtual photon is modified by the presence of quark and gluon fluctuations in the vacuum. Here we compute this LO-HVP contribution $a_\mu^{\text{LO-HVP}}$, using ab initio simulations in QCD and QED. In the present work, we include both QED and QCD in a lattice formulation, including four non-degenerate quark flavors (up, down, strange and charm). We also consider the tiny contributions of the bottom and top quarks.

We compute $a_\mu^{\text{LO-HVP}}$ in the time-momentum representation [3], therefore we need the following two-point function in Euclidean time t:

$$G(t) = \frac{1}{3e^2} \sum_{\mu=1,2,3} \int d^3x \langle J_\mu(\vec{x}, t) J_\mu(0) \rangle \,, \tag{1}$$

where J_μ is the electromagnetic current of quarks with $J_\mu/e = \frac{2}{3}\bar{u}\gamma_\mu u - \frac{1}{3}\bar{d}\gamma_\mu d - \frac{1}{3}\bar{s}\gamma_\mu s + \frac{2}{3}\bar{c}\gamma_\mu c$. u, d, s and c are the up, down, strange and charm quark fields and the angle brackets stand for the QCD+QED expectation value to order e^2. It is useful to decompose $G(t)$ into light, strange, charm and disconnected components, since they have very different statistical and systematic uncertainties. Integrating the one-photon-irreducible (1γI) part of the two-point function (1) yields the LO-HVP contribution to the magnetic moment of the muon [3–6]:

$$a_\mu^{\text{LO-HVP}} = \alpha^2 \int_0^\infty dt\, K(t)\, G_{1\gamma\text{I}}(t) \,, \tag{2}$$

with the weight function,

$$K(t) = \int_0^\infty \frac{dQ^2}{m_\mu^2}\, \omega\left(\frac{Q^2}{m_\mu^2}\right)\left[t^2 - \frac{4}{Q^2}\sin^2\left(\frac{Qt}{2}\right)\right] , \tag{3}$$

and where $\omega(r) = [r + 2 - \sqrt{r(r+4)}]^2/\sqrt{r(r+4)}$, α is the fine structure constant in the Thomson limit and m_μ is the muon mass. We are computing only the LO-HVP contribution, therefore we drop the superscript for brevity and multiply the result by 10^{10}.

The subpercent precision, that we are aiming for, represents a huge challenge for lattice QCD. In order to reach that goal, we have to address the following critical issues: scale determination; QED and strong-isospin breaking; noise reduction; infinite-volume and continuum extrapolations. We briefly discuss these one by one. For a more detailed exposition we refer the reader to the Supplementary Information in [7].

*e-mail: btoth@uni-wuppertal.de

2 Scale determination

The quantity a_μ depends on the muon mass. When computing (2) on the lattice, m_μ has to be converted into lattice units, am_μ, where a is the lattice spacing. A relative error of the lattice spacing propagates into about a twice as large a relative error on a_μ, so that a has to be determined with a few permil precision. We use the mass of the Ω^- baryon, $M_{\Omega^-} = 1672.45(29)$ MeV [8], to set the lattice spacing.

To extract the mass of the positive-parity, ground-state Ω baryon, we are using the operator [9]

$$\Omega_{\rm VI}(t) = \sum_{x_k \text{ even}} \epsilon_{abc} \left[S_{1\chi_a} S_{12\chi_b} S_{13\chi_c} - S_{2\chi_a} S_{21\chi_b} S_{23\chi_c} + S_{3\chi_a} S_{31\chi_b} S_{32\chi_c} \right](x). \quad (4)$$

Here, $\chi_a(x)$ is the strange-quark field with color index a, and the operator S_μ performs a symmetric, gauge-covariant shift in direction μ, while $S_{\mu\nu} \equiv S_\mu S_\nu$.

On the Ω propagators we perform a four-state fit using the fit function h, with two positive and two negative parity states:

$$h(t, A, M) = A_0 h_+(M_0, t) + A_1 h_-(M_1, t) + A_2 h_+(M_2, t) + A_3 h_-(M_3, t) \quad (5)$$

with $h_+(M, t) = e^{-Mt} + (-1)^{t-1} e^{-M(T-t)}$ and $h_-(M, t) = -h_+(M, T-t)$ describing the time dependence of the positive and negative parity states. Here M_0 and A_0 are the mass and amplitude of the ground state. In order to stabilize the fit, a prior term was introduced, containing priors on the masses except for the ground state. The prior for the negative parity ground state, $M_1 = 2012$ MeV, is motivated by the recent observation from the Belle collaboration [10]. The excited states, $M_2 = 2250$ MeV and $M_3 = 2400$ MeV, have not been discovered in experiments so far, so their priors follow from the quark model [11].

In addition to the above four-state fit to the Ω propagator we also used a mass extraction procedure proposed in [12], which is based on the Generalized Eigenvalue Problem (GEVP). The method has the advantage of not using priors. For each time slice t we construct a 4×4 matrix $\mathcal{H}_{i,j}(t) = H_{t+(i-1)+(j-1)}$ $(i, j = 1, \ldots, 4)$, from the hadron propagator H_t. Then for a given t_a and t_b let $\lambda(t_a, t_b)$ be an eigenvalue and $v(t_a, t_b)$ an eigenvector solution to this 4×4 generalized eigenvalue problem:

$$\mathcal{H}(t_a) v(t_a, t_b) = \lambda(t_a, t_b) \mathcal{H}(t_b) v(t_a, t_b). \quad (6)$$

Here we select the smallest eigenvalue λ and use the corresponding eigenvector v to project out the ground state:

$$v^+(t_a, t_b) \mathcal{H}(t) v(t_a, t_b), \quad (7)$$

which then can be fitted to a simple $\exp(-Mt)$ type function.

The mass extracted using the GEVP gives a third M_Ω value for each ensemble, beside the results with the four-state fit procedure with two fit ranges. We will use the deviation between these three values as a systematic error in the Ω mass determination.

3 Isospin-breaking effects

Our staggered path integral includes four flavors of quarks, $f = \{u, d, s, c\}$, gluon fields U and photon fields A and is given by:

$$Z = \int [dU] \exp(-S_g[U]) \int [dA] \exp(-S_\gamma[A]) \times \prod_f \det M^{1/4}[V_U \exp(ieq_f A), m_f]. \quad (8)$$

The photon integral measure $[dA]$ and action S_γ are defined in the QED_L scheme [13]. The one-hop staggered matrix in a background field W_μ can be written as

$$M[W, m] = D[W] + m = \sum_\mu D_\mu[W_\mu] + m, \quad (9)$$

where D_μ is the covariant differentiation in the μ direction involving W and its adjoint $W^\dagger$ together with the obligatory staggered phases. In the path integral the fermions are coupled to a gauge field that is a product of the exponentiated photon field and of the smeared gluon gauge field V_U. $q_f \in \{+\frac{2}{3}, -\frac{1}{3}, -\frac{1}{3}, +\frac{2}{3}\}$ stand for the quark electric charges in units of the positron charge e, m_f for the quark masses and $\alpha = e^2/(4\pi)$. We use the notation $\delta m \equiv m_d - m_u$ for the difference in the up and down quark masses and $m_l \equiv \frac{1}{2}(m_u + m_d)$ for their average. To simplify later formulas we also introduce the notations

$$M_f \equiv M[V_U e^{ieq_f A}, m_f], \quad (10)$$

$$\text{dets}[U, A; \{m_f\}, \{q_f\}, e] \equiv \prod_f \det M_f^{1/4}, \quad (11)$$

where the latter is the product of all fermion determinants.

In this work isospin-breaking is implemented by taking derivatives with respect to the isospin-breaking parameters and by measuring the so obtained derivative operators on isospin-symmetric configurations [14]. We introduce a set of notations for isospin-symmetric observables and their isospin-breaking derivatives. Consider the observable $X(e, \delta m)$, which is a function of e and δm. Then we define

$$X_0 \equiv X(0,0), \qquad X'_m \equiv m_l \frac{\partial X}{\partial \delta m}(0,0),$$
$$X'_1 \equiv \frac{\partial X}{\partial e}(0,0), \qquad X''_2 \equiv \frac{1}{2}\frac{\partial^2 X}{\partial e^2}(0,0). \quad (12)$$

We take into account only leading-order isospin-breaking in this work, so no higher derivatives are needed.

In the case of the fermion determinant, the isospin-symmetric value is denoted by dets_0. Since dets is symmetric under the exchange $u \leftrightarrow d$, the strong-isospin-breaking of dets is zero at leading order: $\text{dets}'_m = 0$. The electromagnetic derivatives are

$$\frac{\text{dets}'_1}{\text{dets}_0} = \sum_f \frac{q_f}{4} \text{Tr}\left(M_f^{-1} D[iAV_U]\right), \quad (13)$$

$$\frac{\text{dets}''_2}{\text{dets}_0} = \frac{1}{2}\left[\left(\frac{\text{dets}'_1}{\text{dets}_0}\right)^2 - \sum_f \frac{q_f^2}{4} \text{Tr}\left(M_f^{-1} D[A^2 V_U]\right) - \sum_f \frac{q_f^2}{4} \text{Tr}\left(M_f^{-1} D[iAV_U] M_f^{-1} D[iAV_U]\right)\right],$$

where Tr is trace over color and spacetime indices and the argument of the D operator is a 3×3 complex matrix valued field, e.g. $A^2 V_U$ has components $A^2_{\mu,x}[V_U]_{\mu,x}$.

We also make a distinction between the electric charge in the fermion determinant and in the operator that we measure. We call the former sea electric charge and denote it by e_s, the latter is the valence electric charge and is denoted by e_v. For an observable X that depends on both the valence and sea charges, $X(e_v, e_s)$, the second order electric charge derivatives are defined as $X''_{20} \equiv \frac{1}{2}\frac{\partial^2 X}{\partial e_v^2}(0,0)$, $X''_{11} \equiv \frac{\partial^2 X}{\partial e_v \partial e_s}(0,0)$, $X''_{02} \equiv \frac{1}{2}\frac{\partial^2 X}{\partial e_s^2}(0,0)$. For functions that depend on either e_v or e_s, but not on both, we use the single digit notations of Equation (3).

The expectation value of an operator O is calculated by inserting $O[U, A]$ into the integrand of the path integral of Equation (8) and normalizing the integral by Z. Here we consider operators whose photon field dependence arises entirely from the photon-quark interaction, i.e. $O = O[U, e_v A]$. The expectation value of this operator depends on δm, e_v and e_s, and the expansion in isospin breaking corrections can be written as:

$$\langle O \rangle = [\langle O \rangle]_0 + e_v^2 \langle O \rangle''_{20} + e_v e_s \langle O \rangle''_{11} + e_s^2 \langle O \rangle''_{02} + \frac{\delta m}{m_l} \langle O \rangle'_m . \tag{14}$$

Here, the individual terms can be expressed as expectation values obtained with the isospin-symmetric path integral, which we denote by $\langle \ldots \rangle_0$. The concrete expressions are:

$$\begin{aligned}
\text{iso:} \quad & [\langle O \rangle]_0 = \langle O_0 \rangle_0 \\
\text{val-val:} \quad & \langle O \rangle''_{20} = \langle O''_2 \rangle_0 \\
\text{sea-val:} \quad & \langle O \rangle''_{11} = \left\langle O'_1 \frac{\text{dets}'_1}{\text{dets}_0} \right\rangle_0 \\
\text{sea-sea:} \quad & \langle O \rangle''_{02} = \left\langle O_0 \frac{\text{dets}''_2}{\text{dets}_0} \right\rangle_0 - \langle O_0 \rangle_0 \left\langle \frac{\text{dets}''_2}{\text{dets}_0} \right\rangle_0 \\
\text{sib:} \quad & \langle O \rangle'_m = \langle O'_m \rangle_0
\end{aligned} \tag{15}$$

In the derivation of these expressions we use $\left\langle \frac{\text{dets}'_1}{\text{dets}_0} \right\rangle_0 = 0$.

Note that Equation (14) is an expansion in bare parameters and not what we consider a decomposition into isospin-symmetric and isospin breaking parts. The latter involves derivatives with respect to renormalized observables and our prescription for that is given in Section 3.1. There is no need to introduce a renormalized electromagnetic coupling though: its running is an $O(e^4)$ effect, i.e. beyond the leading order isospin approximation that we consider here.

3.1 Isospin-breaking decomposition

For various purposes it is useful to decompose the observables into isospin-symmetric and isospin-breaking parts. This requires a matching of the isospin symmetric and full theories, in which we specify a set of observables that must be equal in both theories. Of course, different sets will lead to different decompositions, which is commonly referred to as scheme dependence. Only the sum of the components, i.e. the result in the full theory, is scheme independent.

A possible choice for the observables are the Wilson-flow–based w_0 scale and the masses of mesons built from an up/down/strange and an anti-up/down/strange quark, $M_{uu}/M_{dd}/M_{ss}$. These mesons are defined by taking into account only the quark-connected contributions in their two-point functions [15]. Their masses are practical substitutes for the quark masses. Also, they are neutral and have no magnetic moment, so they are a reasonable choice for an isospin decomposition. These masses cannot be measured in experiments, but have a well defined continuum limit and thus a physical value can be associated to them. In particular, we use the combinations $M^2_{\pi_\chi} \equiv \frac{1}{2}(M^2_{uu} + M^2_{dd})$ and $\Delta M^2 \equiv M^2_{dd} - M^2_{uu}$. For the determination of the physical values of w_0, M_{ss} and ΔM^2, see the Supplementary Information of [7].

For the decomposition we start with the QCD+QED theory and parameterize our observable $\langle O \rangle$ with the quantities defined above:

$$\langle O \rangle (M_{\pi_\chi} w_0, M_{ss} w_0, \tfrac{L}{w_0}, \Delta M w_0, e) \, . \tag{16}$$

Here, the continuum limit is assumed. We can isolate the electromagnetic part by switching off the electromagnetic coupling, while keeping the other parameters fixed. The strong-isospin-breaking part is given by the response to the ΔM parameter, and the isospin-symmetric part is just the remainder:

$$\langle O \rangle_{\text{qed}} \equiv e^2 \cdot \left. \frac{\partial \langle O \rangle}{\partial e^2} \right|_{M_{\pi_\chi} w_0, M_{ss} w_0, \frac{L}{w_0}, \Delta M w_0, e=0} \tag{17}$$

$$\langle O \rangle_{\text{sib}} \equiv (\Delta M w_0)^2 \cdot \left. \frac{\partial \langle O \rangle}{\partial (\Delta M w_0)^2} \right|_{M_{\pi_\chi} w_0, M_{ss} w_0, \frac{L}{w_0}, \Delta M w_0 = 0, e=0} \tag{18}$$

$$\langle O \rangle_{\text{iso}} \equiv \langle O \rangle (M_{\pi_\chi} w_0, M_{ss} w_0, \tfrac{L}{w_0}, 0, 0). \tag{19}$$

One can also define the decomposition at a finite lattice spacing, for which w_0 in lattice units can be additionally fixed. In doing so the isospin symmetric part $\langle O \rangle_{\text{iso}}$ has to be distinguished from the value of the observable at the bare isospin-symmetric point $[\langle O \rangle]_0$.

4 Noise reduction techniques

In this section we describe the measurement techniques that were implemented for the isospin symmetric component of the connected light quark contribution, C_0^{light}. They play a key role in reducing the final statistical error in a_μ. For further details we refer to Ref. [7].

4.1 Low Mode Averaging

The technique utilizes the lowest eigenmodes of the fermion matrix; for an early work with low eigenmodes, see [16]. The way in which we use these modes here is essentially the same as in [17], where it is called Low Mode Substitution. In the space orthogonal to these modes, the computational effort is reduced considerably by applying imprecise (aka. sloppy) matrix inversions. This is called the Truncated Solver Method [18] or All Mode Averaging [19].

We consider the connected current propagator for timelike separation, and perform an averaging over the source positions, together with a zero spatial-momentum projection at the sink:

$$C(t,\bar{t}) = -\frac{1}{12L^3}\sum_{\mu=1,2,3}\mathrm{ReTr}\left[\mathcal{D}_{\mu,t}M^{-1}\mathcal{D}_{\mu,\bar{t}}M^{-1}\right], \quad (20)$$

where $\mathcal{D}_{\mu,t} = \sum_{\vec{x}} D_\mu[iP_x U]$ is an operator that performs a symmetric, gauge-covariant shift on a vector v_x:

$$[\mathcal{D}_{\mu,t}v]_x = i\eta_{\mu,x}\left(U_{\mu,x}v_{x+\mu} + U^\dagger_{\mu,x-\mu}v_{x-\mu}\right)\cdot\delta_{x_4,t}\,, \quad (21)$$

where $\eta_{\mu,x}$ are the staggered phases. We use the simplifying notation $\mathcal{D} = \mathcal{D}_{\mu,t}$ and $\overline{\mathcal{D}} = \mathcal{D}_{\mu,\bar{t}}$ in the following. In Equation (20), we apply the real part to reduce noise, because the imaginary part vanishes anyway after averaging over gauge configurations.

Using the lowest eigenmodes of M we split the quark propagator into an eigenvector part and into its orthogonal complement, $M^{-1} = M_e^{-1} + M_r^{-1}$, with

$$M_e^{-1} = \sum_i \frac{1}{\lambda_i}v_i v_i^\dagger, \quad M_r^{-1} = M^{-1}\left(1 - \sum_i v_i v_i^\dagger\right), \quad (22)$$

where v_i/λ_i is the i-th eigenvector/eigenvalue of the operator M. Correspondingly, C splits into eigen-eigen, rest-eigen and rest-rest contributions:

$$C = C_{ee} + C_{re} + C_{rr} = -\frac{1}{4L^3}\sum_{\substack{p=e,r\\q=e,r}}\mathrm{ReTr}\left[\mathcal{D}M_p^{-1}\overline{\mathcal{D}}M_q^{-1}\right], \quad (23)$$

where an average over μ is assumed but not shown explicitely. The benefit of this decomposition is that the trace in the **eigen-eigen part** can be calculated exactly, and is thus equivalent to calculating the propagator with all possible sources in position space. This is the main ingredient for the noise reduction. Though no extra inversions are needed in this part, it has to be optimized carefully, since there is a double sum over the eigenmodes, where each term is a scalar product $v_i^\dagger\mathcal{D}v_j$. In the **rest-eigen part** we have terms $v_i^\dagger\mathcal{D}M_r^{-1}\overline{\mathcal{D}}v_i$ and also terms where $\mathcal{D}$ and $\overline{\mathcal{D}}$ are exchanged. Therefore, this part is only a single sum over the eigenmodes, and each term involves one matrix inversion. Note that these inversions are preconditioned by the eigenvectors, so they need many fewer iterations than standard inversions. Additionally, we speed up the inversions by running them with a reduced precision, and for some randomly selected eigenvectors we correct for the small bias by adding the difference between a high precision solver and the reduced precision one [18, 19]. Finally, the **rest-rest part** is evaluated using random source vectors ξ: we calculate $\xi^\dagger\mathcal{D}M_r^{-1}\overline{\mathcal{D}}M_r^{-1}\xi$, which requires two inversions per random source. The reduced precision inverter technique is used here too. The improvement achieved by these noise reduction techniques is shown in Figure 1.

4.2 Upper and lower bounds on $\langle JJ\rangle$

In the case of the light and disconnected contributions to the current propagator, the signal deteriorates quickly as distance is increased. To calculate the HVP, a sum over time of the propagator has to be performed. As was suggested in [21, 22], we introduce a cut in time t_c, beyond which the propagator is replaced by upper and lower bounds, thereby reducing the statistical noise. Our estimate is given by the average of the bounds at a t_c where the two bounds meet. The bounds are derived from the fact that the current propagator is a sum of exponentials with positive coefficients.

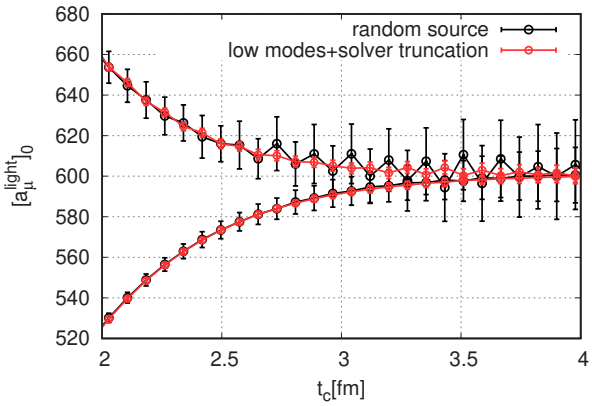

Figure 1. Comparison of a conventional random source based technique, as we applied it in our earlier work [20], and the low-mode improvement technique of this work on a $\beta = 3.9200$ `4stout` ensemble for the case of $[a_\mu^{light}]_0$'s upper and lower bounds (see Section 4.2).

For the light connected propagator at the isospin-symmetric point the bounds express the positivity (lower bound) and that the propagator should decay faster than the exponential of two pions (upper bound). They are given as

$$0 \le G^{light}(t) \le G^{light}(t_c)\frac{\varphi(t)}{\varphi(t_c)}, \quad (24)$$

where $\varphi(t) = \exp(-E_{2\pi}t)$. For $E_{2\pi}$ we use the energy of two non-interacting pions with the smallest non-zero lattice momentum $2\pi/L$. The larger the t_c the better the upper bound, but it comes with more statistical noise.

The exponential decay above assumes an infinite time extent, $T = \infty$. We incorporate the effects of a finite-T using next-to-leading-order chiral perturbation theory. There the exponential decay with the two-pion energy gets replaced by the following cosh-type form:

$$\exp(-E_{2\pi}t) \longrightarrow \frac{\cosh[E_{2\pi}(t - T/2)] + 1}{\cosh(E_{2\pi}T/2) - 1}\,. \quad (25)$$

5 Finite-size effects

We compute finite-size effects on a_μ in a systematic way, which includes dedicated lattice simulations, chiral perturbation theory and phenomenological models. The concrete goal is to provide a single number that is to be added to the continuum-extrapolated lattice result obtained in

a reference box, which is defined by a spatial extent of $L_{\rm ref} = 6.272$ fm and a temporal extent of $T_{\rm ref} = \frac{3}{2}L_{\rm ref}$.

We perform dedicated lattice simulations with two different lattice geometries: one is a 56×84 lattice with the reference box size and the other is a large 96×96 lattice with box size $L = L_{\rm big} = 10.752$ fm and $T = T_{\rm big} = L_{\rm big}$. Since taste violations distort the finite-size effects, we designed a new action with highly-suppressed taste breaking, which we call 4HEX (see [7]). Our strategy is then to compute the finite-size correction as the following sum:

$$\begin{aligned} a_\mu(\infty,\infty) - a_\mu(L_{\rm ref}, T_{\rm ref}) &= \\ &= [a_\mu(L_{\rm big}, T_{\rm big}) - a_\mu(L_{\rm ref}, T_{\rm ref})]_{\rm 4HEX} \\ &\quad + [a_\mu(\infty,\infty) - a_\mu(L_{\rm big}, T_{\rm big})]_{\rm XPT}. \end{aligned} \quad (26)$$

The first difference on the right hand side is taken from the dedicated 4HEX simulations. The second difference is expected to be much smaller than the first and is taken from a non-lattice approach: two-loop chiral perturbation theory.

We consider four non-lattice approaches to compute both differences on the right hand side of Equation (26). In the case of the first difference, the results obtained are compared to our 4HEX simulations. The first approach is chiral perturbation theory (XPT) to next-to-leading and next-to-next-to-leading orders (NLO and NNLO), the second is the Meyer-Lellouch-Luscher-Gounaris-Sakurai model (MLLGS), the third approach is that of Hansen and Patella (HP) [23] and the fourth is the rho-pion-gamma model of [24], which we abbreviate as RHO here.

We compute the first difference in Equation (26) using dedicated simulations with the 4HEX action. We use the harmonic-mean-square (HMS) to set the physical point:

$$M_{\pi,\rm HMS}^{-2} \equiv \frac{1}{16}\sum_\alpha M_{\pi,\alpha}^{-2}\,, \quad (27)$$

defined as an average over the masses of the 16 pion tastes, $M_{\pi,\alpha}$. We set $M_{\pi,\rm HMS}$ to the physical value of the pion mass, which requires lowering the Goldstone-pion mass to 110 MeV. This way of fixing the physical point results in much smaller lattice artefacts than the usual setting with the Goldstone-pion, at least for an observable like the finite-size effect. To generate the 4HEX data set, we performed simulations with two different Goldstone pion masses: $M_\pi = 104$ MeV and 121 MeV. To set the physical point as described above, we perform an interpolation from these two pion masses to $M_\pi = 110$ MeV.

We only have one lattice spacing with the 4HEX action, so the finite-size effects cannot be extrapolated to the continuum limit. We estimate the cutoff effect of the result by comparing $a_\mu^{\rm light}$ with the 4HEX action at this single lattice spacing to the continuum extrapolated 4stout lattice result, both in the $L_{\rm ref}$ volume. The 4HEX result is about 7% larger than the continuum value. Therefore we reduce the measured finite-size effect by 7%, and assign a 7% uncertainty to this correction step. For the difference we get

$$a_\mu(L_{\rm big}, T_{\rm big}) - a_\mu(L_{\rm ref}, T_{\rm ref}) = 18.1(2.0)_{\rm stat}(1.4)_{\rm cont}\,. \quad (28)$$

Table 1. The finite size effects $a_\mu(\text{big}) - a_\mu(\text{ref})$ for the isospin-symmetric component in the various model approaches.

NLO XPT	NNLO XPT	MLLGS	HP	RHO
11.6	15.7	17.8	16.7	15.2

The result includes a $\left(\frac{9}{10}\right)$ charge factor, and the first error is statistical and the second is an estimate of the cutoff effect.

The finite-size effects computed in various non-lattice approaches are collected in Table 1. Except for the NLO result, the different models give finite-size effects of similar size, which agree well with the lattice determination of Equation (28). The good agreement for the finite-size effect in the reference box, between the models and the lattice, gives us confidence that the models can be used to reliably compute the very small, residual, finite-size effect of the large box. As a final value for the large-box, finite-size effect we take the NNLO XPT result including finite-T effects:

$$a_\mu(\infty,\infty) - a_\mu(L_{\rm big}, T_{\rm big}) = 0.6(0.3)_{\rm big}\,, \quad (29)$$

where the uncertainty is an estimate of higher-order effects, given here by the difference of the NNLO and NLO values.

For our final result for the finite-size effect in the reference box, we also include the contribution of isoscalar channel and isospin-breaking effects giving:

$$\begin{aligned} &a_\mu(\infty,\infty) - a_\mu(L_{\rm ref}, T_{\rm ref}) = \\ &= 18.7(2.0)_{\rm stat}(1.4)_{\rm cont}(0.3)_{\rm big}(0.6)_{I=0}(0.1)_{\rm qed}[2.5]\,. \end{aligned} \quad (30)$$

The first error is the statistical uncertainty of our 4HEX computation, the second is an estimate of the 4HEX cutoff effects, the third is the uncertainty of the residual finite-size effect of the "big" lattice, the fourth is a XPT estimate of the $I = 0$ finite size effect and the fifth is an estimate of the isospin-breaking effects. The last, total error in the square-brackets is the sum of the first five, added in quadrature.

6 Taste improvement

As is well known, some of the most important cutoff effects of staggered fermions are taste violations. At long distances, these violations distort the pion spectrum. Since a_μ is predominantly a long-distance observable, dominated by a two-pion contribution, including the ρ resonance, we expect these effects to be largest in the light-quark terms.

We investigate various physically motivated models for reducing long-distance taste violations in our lattice results. We consider three techniques: next-to-next-to-leading order chiral perturbation theory (NNLO XPT), a Meyer-Lellouch-Lüscher-Gounaris-Sakurai model (MLLGS) and the rho-pion-gamma model (RHO). A detailed exposition of these models can be found in the Supplementary Material of Ref. [7]. We investigate and discuss the suitability of their staggered versions for

reducing the taste violations present in our lattice data. We call the resulting corrections taste improvements, because they improve the continuum extrapolation of our lattice data without, in principle, modifying the continuum-limit value. Indeed, these corrections vanish in that limit, as taste-breaking effects should. These improvements are applied on light-quark observables at the isospin-symmetric point, whose taste violations have the largest impact on our final uncertainties.

The models NNLO XPT, MLLGS and RHO describe the long-distance physics associated with finite-volume effects, as measured in our simulations. One can also define corresponding models describing the taste violations, they are denoted NNLO SXPT, SMLLGS and SRHO. We find that they describe the physics associated with taste violations, at least at larger distances. This is illustrated in Figure 2, where cutoff effects in the integrand of $a_\mu^{\rm light}$ are plotted as a function of Euclidean time. More specifically, we define the physical observable, obtained by convoluting the integrand of $a_\mu^{\rm light}$ with a smooth window function

$$W(t;t_1,t_2) \equiv \Theta(t;t_1,\Delta) - \Theta(t;t_2,\Delta) \tag{31}$$

with

$$\Theta(t;t',\Delta) \equiv \tfrac{1}{2} + \tfrac{1}{2}\tanh[(t-t')/\Delta], \tag{32}$$

having a width of $t_2 - t_1 = 0.5$ fm and starting at a time of t_1. Then we consider the difference in the value of this observable, obtained on a fine and a coarse lattice at a sequence of t_1 separated by 0.1 fm. These are compared to the NLO SXPT, NNLO SXPT, SRHO and SMLLGS predictions for this quantity, evaluated at the exact parameters of the ensembles.

The SMLLGS, the SRHO and the NNLO SXPT taste improvements describe the numerical data very nicely for $t_1 \gtrsim 2.0$ fm, fairly well for $t_1 \gtrsim 1.0$ fm and all the way down to $t_1 \simeq 0.4$ fm in the case of SRHO. All three slightly overestimate the observed cutoff effects, the rho-meson based approach performing best, whereas NNLO displays a large deviation from the lattice results in the $t_1 \leq 0.8$ fm region. The lattice results have a maximum at $t_1 = 1.4$ fm, as does the SRHO improvement, reinforcing our confidence that this model captures the relevant physics.

These findings lead us to apply the following taste corrections to our simulations results for $a_\mu^{\rm light}(L,T,a)$, obtained on an $L^3 \times T$ lattice with lattice spacing a, before performing continuum extrapolations:

$$\begin{aligned} &a_\mu^{\rm light}(L,T,a) \to \\ &\to a_\mu^{\rm light}(L,T,a) + \tfrac{10}{9}\left[a^{\rm RHO}_{\mu,t\geq t_{\rm sep}}(L_{\rm ref},T_{\rm ref}) - a^{\rm SRHO}_{\mu,t\geq t_{\rm sep}}(L,T,a)\right], \end{aligned} \tag{33}$$

with $t_{\rm sep} = 0.4, 0.7, 1.0, 1.3$ fm, and where the factor (10/9) is related to the quark charges. Note that by using $L_{\rm ref}$ and $T_{\rm ref}$ in the above Equation, we are applying a very small volume correction to interpolate all of our simulation results to the same reference, four-volume so that they can be extrapolated to the continuum limit together.

The taste-improved data is then extrapolated to the continuum using our standard fit procedure, in the course of which isospin-breaking effects are also included. For estimating the systematic error we use a histogram technique [7].

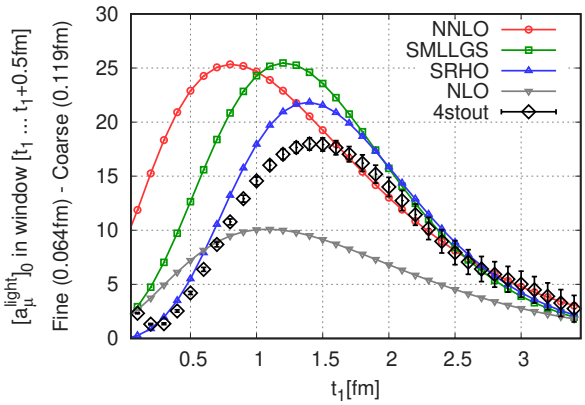

Figure 2. Isospin-symmetric component of $a_\mu^{\rm light}$ computed with a sliding window. The window starts at t_1 and ends 0.5 fm later. The plot shows the difference between a fine and a coarse lattice, whose sizes are $L = 6.14$ fm and $L = 6.67$ fm. The black squares with errors are obtained from the simulation. The colored curves are the predictions of NLO and NNLO SXPT, the SRHO and the SMLLGS models. They are computed at the parameters (pion mass, taste violation, volume) of the simulations.

The procedure described above does not yet take into account the systematic uncertainty associated with our choice of SRHO for taste improvement for $t > 1.3$ fm. Since applying no taste improvement in that region is not an option, because of the nonlinearities introduced by two-pion, taste violations, we turn to NNLO SXPT, only as a means to estimate the uncertainty associated with this choice. Thus, we define this systematic uncertainty as ERR = (SRHO − NNLO SXPT) for $t > 1.3$ fm. Then, we perform the same histogram analysis but with SRHO, SRHO-ERR and SRHO+ERR improvements. From this histogram we extract the contribution which comes from the variation in the improvement model from SRHO-ERR to SRHO+ERR. We assign this full spread to the systematic uncertainty associated with the taste-improvement procedure. We add this error in quadrature to the error given by the histogram technique discussed in the previous paragraph.

7 Intermediate window

The work [21] defined a particularly useful observable $a_{\mu,\rm win}$, in which the current propagator is restricted to a time window $[t_1,t_2]$, using the smooth weight function $W(t;t_1,t_2)$ defined in Equation (31). The advantage of $a_{\mu,\rm win}$ over a_μ is that, by choosing an appropriate window, the calculation can be made much less challenging on the lattice than for the full a_μ. Here we will be interested in the window between $t_1 = 0.4$ fm and $t_2 = 1.0$ fm, i.e. in an intermediate time range. By this choice we eliminate both the short-distance region, where large cutoff effects are present, and the long-distance region, where the statis-

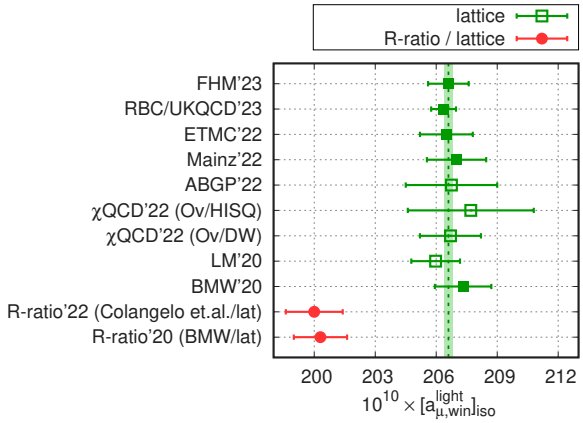

Figure 3. Isospin-symmetric, light, connected component of the window observable, $[a^{\rm light}_{\mu,\rm win}]_{\rm iso}$. The green squares denote the lattice results. From each group only the most recent values are shown: FHM'23 [26], RBC/UKQCD'23 [27], ETMC'22 [28], Mainz'22 [29], ABGP'22 [30], χQCD'22 with overlap valence on HISQ and overlap valence on domain wall configurations [31], LM'20 [32], and our result BMW'20 [7]. The data points with filled squares give a set of independent results: each of these are obtained using a different set of configurations. The green vertical band represents their weighted average. The red dots show the R-ratio based determinations. They are obtained by combining results from the data-driven approach for $a_{\mu,\rm win}$ and lattice results for the non-light-connected contributions, as described in [7]. The averaged lattice result is 4.8 sigmas away from the value of R-ratio'20 (BMW/lat) [7], and 4.7 sigmas away from the result R-ratio'22 (Colangelo et.al./lat) [25].

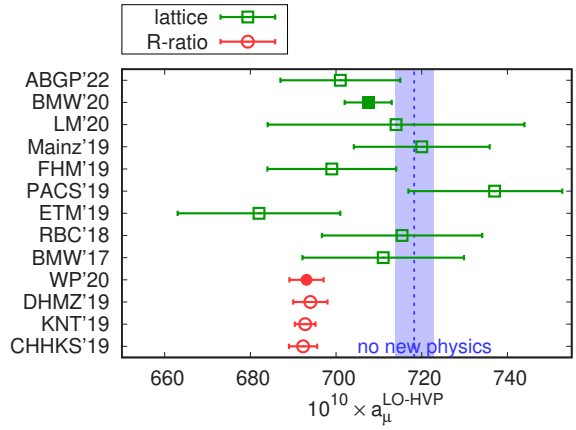

Figure 4. Comparison of recent results for the leading-order, hadronic vacuum polarization contribution to the anomalous magnetic moment of the muon. Green squares are lattice results: this work's result, BMW'20, is represented by a filled symbol. The open squares show other lattice results: ABGP'22 [30], LM'20 [32], Mainz'19 [33], FHM'19 [34], ETM'19 [35], RBC'18 [21] and our earlier work BMW'17 [20]. Red circles were obtained using the R-ratio method: the combined result WP'20 [36] is followed by DHMZ'19 [37], KNT'19 [38] and CHHKS'19 [39, 40]; these results use the same experimental data as input. The blue shaded region is the value that $a_\mu^{\rm LO-HVP}$ would have to have to explain the experimental measurement of $(g_\mu - 2)$, assuming no new physics.

tical uncertainties and finite-size effects are large. Moreover, in the case of staggered fermions, it has reduced taste-breaking artefacts.

On the other hand, $a_{\mu,\rm win}$ can be computed in the R-ratio approach [7, 25] as well, which can then be compared to the values obtained on the lattice, providing a sharp comparison of the two methods.

The isospin-symmetric component of the connected, light, window quantity, $[a^{\rm light}_{\mu,\rm win}]_{\rm iso}$, has been computed by several lattice groups. The most recent value from each group is collected in Figure 3. The average of the most recent, independent lattice determinations show a 4.8 σ and a 4.7 σ tension compared to the R-ratio-based determinations of [7] and [25], respectively.

8 Conclusions

Combining all of these ingredients we obtain, as a final result, $a_\mu = 707.5(2.3)(5.0)[5.5]$. The first, statistical error comes mostly from the noisy, large-distance region of the current-current correlator. The second, systematic error is dominated by the continuum extrapolation and the finite-size effect computation. The third, total error is obtained by adding the first two in quadrature. In total we reach a relative accuracy of 0.8%.

Figure 4 compares our result with previous lattice computations and also with results from the R-ratio method, which have recently been reviewed in [36]. As one can see, there is a tension between our result and those obtained by the R-ratio method. For the total, LO-HVP contribution to a_μ, our result is 2.0σ, 2.5σ, 2.4σ and 2.2σ larger than the R-ratio results of $a_\mu = 694.0(4.0)$ [37], $a_\mu = 692.78(2.42)$ [38], $a_\mu = 692.3(3.3)$ [39, 40] and the combined result $a_\mu = 693.1(4.0)$ of [36], respectively. It is worth noting that the R-ratio determinations are based on the same experimental data sets and are therefore strongly correlated, though these data sets were obtained in several different and independent experiments that we have no reason to believe are collectively biased. Clearly, these comparisons need further investigation.

To conclude, when combined with the other standard model contributions (see eg. [36]), our result for the leading-order hadronic contribution to the anomalous magnetic moment of the muon, weakens the longstanding discrepancy between experiment and theory. However, as discussed above and can be seen in Figure 4, our lattice result shows some tension with the R-ratio determinations. Obviously, our findings should be confirmed –or refuted– by other collaborations using other discretizations of QCD.

References

[1] G.W. Bennett et al. (Muon g-2), Phys. Rev. **D73**, 072003 (2006), `hep-ex/0602035`

[2] B. Abi et al. (Muon g-2), Phys. Rev. Lett. **126**, 141801 (2021), `2104.03281`

[3] D. Bernecker, H.B. Meyer, Eur. Phys. J. **A47**, 148 (2011), 1107.4388
[4] B.E. Lautrup, A. Peterman, E. de Rafael, Phys. Rept. **3**, 193 (1972)
[5] E. de Rafael, Phys. Lett. **B322**, 239 (1994), hep-ph/9311316
[6] T. Blum, Phys. Rev. Lett. **91**, 052001 (2003), hep-lat/0212018
[7] S. Borsanyi et al., Nature **593**, 51 (2021), 2002.12347
[8] M. Tanabashi et al. (Particle Data Group), Phys. Rev. **D98**, 030001 (2018)
[9] M.F.L. Golterman, J. Smit, Nucl. Phys. **B255**, 328 (1985)
[10] J. Yelton et al. (Belle), Phys. Rev. Lett. **121**, 052003 (2018), 1805.09384
[11] S. Capstick, N. Isgur, Phys. Rev. **D34**, 2809 (1986), [AIP Conf. Proc.132,267(1985)]
[12] C. Aubin, K. Orginos, AIP Conf. Proc. **1374**, 621 (2011), 1010.0202
[13] M. Hayakawa, S. Uno, Prog. Theor. Phys. **120**, 413 (2008), 0804.2044
[14] G.M. de Divitiis, R. Frezzotti, V. Lubicz, G. Martinelli, R. Petronzio, G.C. Rossi, F. Sanfilippo, S. Simula, N. Tantalo (RM123), Phys. Rev. **D87**, 114505 (2013), 1303.4896
[15] S. Borsanyi et al. (Budapest-Marseille-Wuppertal), Phys. Rev. Lett. **111**, 252001 (2013), 1306.2287
[16] H. Neff, N. Eicker, T. Lippert, J.W. Negele, K. Schilling, Phys. Rev. **D64**, 114509 (2001), hep-lat/0106016
[17] A. Li et al. (xQCD), Phys. Rev. **D82**, 114501 (2010), 1005.5424
[18] G.S. Bali, S. Collins, A. Schafer, Comput. Phys. Commun. **181**, 1570 (2010), 0910.3970
[19] T. Blum, T. Izubuchi, E. Shintani, Phys. Rev. **D88**, 094503 (2013), 1208.4349
[20] S. Borsanyi et al. (Budapest-Marseille-Wuppertal), Phys. Rev. Lett. **121**, 022002 (2018), 1711.04980
[21] T. Blum, P.A. Boyle, V. Gulpers, T. Izubuchi, L. Jin, C. Jung, A. Juttner, C. Lehner, A. Portelli, J.T. Tsang (RBC, UKQCD), Phys. Rev. Lett. **121**, 022003 (2018), 1801.07224
[22] S. Borsanyi, Z. Fodor, T. Kawanai, S. Krieg, L. Lellouch, R. Malak, K. Miura, K.K. Szabo, C. Torrero, B.C. Toth, Phys. Rev. **D96**, 074507 (2017), 1612.02364
[23] M.T. Hansen, A. Patella, Phys. Rev. Lett. **123**, 172001 (2019), 1904.10010
[24] B. Chakraborty, C.T.H. Davies, P.G. de Oliviera, J. Koponen, G.P. Lepage, R.S. Van de Water, Phys. Rev. **D96**, 034516 (2017), 1601.03071
[25] G. Colangelo, A.X. El-Khadra, M. Hoferichter, A. Keshavarzi, C. Lehner, P. Stoffer, T. Teubner, Phys. Lett. B **833**, 137313 (2022), 2205.12963
[26] A. Bazavov et al. (2023), 2301.08274
[27] T. Blum et al. (2023), 2301.08696
[28] C. Alexandrou et al. (2022), 2206.15084
[29] M. Cè et al., Phys. Rev. D **106**, 114502 (2022), 2206.06582
[30] C. Aubin, T. Blum, M. Golterman, S. Peris, Phys. Rev. D **106**, 054503 (2022), 2204.12256
[31] G. Wang, T. Draper, K.F. Liu, Y.B. Yang (chiQCD) (2022), 2204.01280
[32] C. Lehner, A.S. Meyer, Phys. Rev. D **101**, 074515 (2020), 2003.04177
[33] A. Gerardin, M. Ce, G. von Hippel, B. Horz, H.B. Meyer, D. Mohler, K. Ottnad, J. Wilhelm, H. Wittig, Phys. Rev. **D100**, 014510 (2019), 1904.03120
[34] C.T.H. Davies et al. (Fermilab Lattice, LATTICE-HPQCD, MILC), Phys. Rev. **D101**, 034512 (2020), 1902.04223
[35] D. Giusti, V. Lubicz, G. Martinelli, F. Sanfilippo, S. Simula, Phys. Rev. **D99**, 114502 (2019), 1901.10462
[36] T. Aoyama et al., Phys. Rept. **887**, 1 (2020), 2006.04822
[37] M. Davier, A. Hoecker, B. Malaescu, Z. Zhang, Eur. Phys. J. C **80**, 241 (2020), 1908.00921
[38] A. Keshavarzi, D. Nomura, T. Teubner, Phys. Rev. **D101**, 014029 (2020), 1911.00367
[39] G. Colangelo, M. Hoferichter, P. Stoffer, JHEP **02**, 006 (2019), 1810.00007
[40] M. Hoferichter, B.L. Hoid, B. Kubis, JHEP **08**, 137 (2019), 1907.01556